Low Reynolds Number Flow Dynamics of a Thin, Flat Airfoil with Elastically Mounted Trailing Edge

Sourabh V. Apte* and James A. Liburdy†

School of Mechanical, Industrial and Manufacturing Engineering, Oregon State University, Corvallis, OR 97331

Miguel Visbal‡

U.S. Airforce Research Laboratory, Wright Patterson Airforce Base, Dayton, OH 45433-7512

Direct numerical simulations were performed to study the effect of an elastically mounted trailing edge actuator on the unsteady flow over a plunging, thin airfoil at Reynolds number of 14700 based on the chord length. The goal is to investigate potential benefits of flow-induced passive actuation of the trailing edge to the lift and drag characteristics of flapping MAV wings. The trailing edge, of 30% the chord length, is hinged to the wing using a torsion spring. It may undergo flow induced rotation resulting in dynamic variations in the airfoil shape. This trailing-edge spring assembly is modeled by simple, linear, torsion spring dynamics. A small parameter space varying the spring flexibility is explored to investigate its effect on the airfoil performance. Firstly, the second-order fictitious domain based finite volume approach by Apte et al. (J. Comp. Phys. 2009) was extended to model this fluid-structure interaction problem on a fixed, Cartesian mesh. Verification studies were conducted on a canonical test case of a spring-mounted cylinder to show good predictive capability. Secondly, flow over a plunging thin flat airfoil, at reduced frequency of 5.7 (10 Hz) and 5° angle of attack was investigated with and without the actuation of the trailing edge. It was found that, spring natural frequencies higher than the plunging frequency result in the tailing edge actuation that leads to net increase in thrust. The phase difference between the leading and trailing edge motions was found to vary based on the spring flexibility and played a critical role in governing wing performance.

I. Introduction

There is considerable interest in biologically inspired flows with applications to small unmanned vehicles and micro-air vehicles (MAVs).[1–5] Designing efficient and stable MAVs with flapping wings that are easily maneuverable and resistant to flow disturbances is receiving a lot of attention.[6] Considerable effort has been devoted toward flexible wings for such designs, following the bird flight such as bats.[7–9] However, providing fundamental analysis explaining resultant increase in propulsion efficiency or thrust owing to flexibility has been a challenge due to the complexity of the fluid-structure interaction problem. Oscillating foils with chordwise or spanwise flexibility have been studied using experiments[3–5,10,11] as well as simulations[1,12–17] to show positive benefits of flexibility on performance. Trailing edge 'pop-up' studies of Meyer *et al.*[18] and Schluter[19] show that birds use a trailing edge flap that is self-adjusting to reduce trailing edge separation and the result is higher lift and delayed stall at high angle of attack. Even at zero Reynolds numbers (hovering flight conditions), wing flexibility has been shown to provide higher thrust.[11,20–22]

Heathcote and Gursul[5,23] used a plunging teardrop airfoil with a long, slender and flexible filament at the tail to show that there exists a range of flexibility of the trailing edge filament that provides increased thrust and propulsion efficiency. This increase in efficiency is linked to the *phase difference* between the leading edge plunging motion and the trailing edge flapping. Trailing edge flexibility causing a 90° phase difference has been shown to yield the highest increase in efficiency.

*Associate Professor, Mechanical Engineering, Oregon State University, AIAA Member.

†Professor, Mechanical Engineering, Oregon State University, AIAA Member

‡Technical Area Leader, Computational Sciences Division, AFRL/RBAC, Fellow AIAA

Owing to complexities of the unsteady flow and flexible wing interaction, understanding the effect of continuous wing flexibility, with high degrees of freedom, on airfoil performance is difficult. There is a critical need to develop a canonical problem that is simple enough and yet represents the salient features of the wing-flexibility and flow dynamics for fundamental analysis. Recently, Eldredge and co-workers[21,22,24] developed a simplified two-element rigid model of a wing that are hinged through torsion springs to study flapping wing aerodynamics under hovering conditions ($Re = 0$). The torsion spring provides rotational flexibility and the leading element of the wing is driven to undergo translational (plunge) and rotational (pitch) kinematics. This canonical model allowed direct comparison of the computational predictions based on a vortex method to experimental data as quantifying spring parameters is relatively straightforward.

This work investigates a *hinged trailing edge mounted with torsion springs*, to provide a simple yet realistic model for flapping wing design with chordwise flexibility as observed in small birds. As the first step, effects of flow induced actuation on the lift and drag characteristics under plunging motion is investigated. The **central hypotheses** for this work are

- flow-induced, passive actuation of the trailing edge and resultant open loop control combined with plunging motion of the airfoil (representative of flapping wing mechanism), may result in increased thrust and propulsion efficiency for certain range of spring flexibility.;
- appropriate design of the torsion spring may result in flow-induced limit cycle oscillations of the trailing edge and enhance lift-to-drag ratios and performance.

This exploratory study uses thin, flat airfoils as they have been shown to improve lift-to-drag ratios while adhering to weight and size constraints. At low Re, thin flat airfoils actually *delay* stall to higher angles of attack when operating at lower aspect ratios, although the lift is somewhat lower at lower angles of attack.[25] One major concern of thin airfoil design, when operating at high lift conditions, is the unsteady nature of separation at the leading edge resulting in a Kelvin-Helmhotlz type flow instability[26–28] and resultant large unsteadiness in lift and drag characteristics. However, for oscillatory or flapping wings, the angles of attack are typically small and are dynamically changing owing to imposed plunging motions. Thin wings also help maintain lower overall weight of the wings.

Study of a two-dimensional wing is carried out, since it minimizes three-dimensional effects owing to tip vortices which can alter the flow structure in low-aspect ratio wings. A large aspect ratio wing at low Re facilitates use of a two-dimensional DNS approach, significantly saving computational time and facilitating investigation of the flow physics with a wide range of parametric studies. High-fidelity simulations of plunging SD7003 by Visbal[12,13] indicates that transition to turbulence and three-dimensionality effects become important for $Re >$ 30000. In order to test the above hypotheses using numerical techniques, a fictitious domain method developed by Apte *et al*[29] is used, to account for flow-induced oscillations of the trailing edge actuator with one-degree of freedom (rotation around the hinged point). A small parameter space varying the spring flexibility, through its natural frequency (f_N) around the plunging frequency (f_p), is explored to understand its effects on the wing performance.

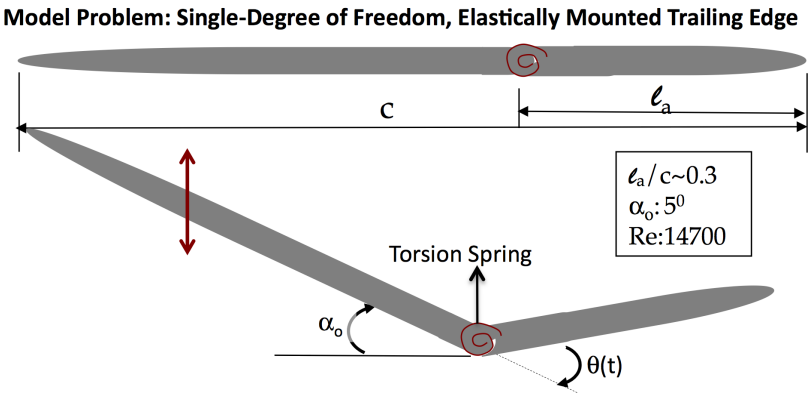

Figure 1. Schematic diagram of a thin, flat wing with a spring-mounted trailing edge actuator.

II. Methodology

The equations for angular motion of the trailing edge with single degree of freedom can be obtained by considering it as a compound pendulum and obtaining the net moment around the hinge location (see figure 2). This includes the moment due to the weight of the trailing edge ($m_a g$), the moment due to the aerodynamic forces on the trailing edge, the restoring moments due to spring, and any pre-tension in the

spring necessary to maintain a mean position aligned with the angle of attack (i.e. $\theta = 0^\circ$) in the absence of any actuation of the trailing edge.

Accordingly, the dimensional equation of motion of the trailing edge is given as,

$$\mathcal{I}_a \frac{d^2\theta}{dt^2} + C\frac{d\theta}{dt} + K\theta + \frac{1}{2} m_a g \ell_a \left(\cos(\theta - \alpha_0)\right) = M_{\text{flow}} - M^{\text{pretension}}, \tag{1}$$

where $\mathcal{I}_a$ is the moment of inertia of the actuator about the hinge, m_a is the mass of the trailing edge actuator, α_0 is the angle of attack, θ is the deflection of the actuator, g is the gravitational acceleration, M_{flow} is the aerodynamic moment on the trailing edge, $M^{\text{pretension}}$ is the moment due to pre-tension in the spring, K and C are the spring stiffness and spring damping parameters, respectively. Note that, spring pretension can be set to obtain the mean position of the trailing edge to align with the angle of attack (i.e. $\theta = 0$) and balances the moment due to the weight of the trailing edge. In order to understand the dynamics of the trailing edge owing to only the aerodynamic forces, further simplification of the above equation is possible, by neglecting the gravity-based term and also the pretension moment in the analysis. These terms were found to have small effect, especially in the case of small values of θ. Using the trailing edge length (ℓ_a) as the length scale and free stream velocity (U_∞) as the velocity scale, the simplified equation can be non-dimensionalized to get,

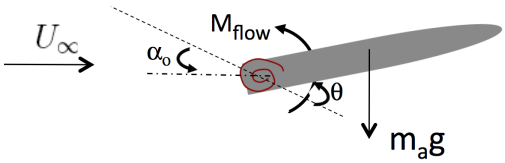

Figure 2. The hinged trailing edge dynamics modeled as a compound pendulum.

$$\frac{d^2\theta}{d\tau^2} + 4\pi\xi St_{\text{N}} \frac{d\theta}{d\tau} + (2\pi St_{\text{N}})^2 \theta \quad = \quad \frac{3}{2\mathcal{I}^*} \left(\frac{\ell_a}{t_a}\right) C_M, \tag{2}$$

where $\mathcal{I}^* = \mathcal{I}_a/(m_f \ell_a^2/3) = \rho_a/\rho_f$ is the moment-of-inertia ratio (ratio of moment of inertia of the actuator about the hinged point to the moment of inertia of the equivalent fluid) which turns out to be the ratio of the actuator density to the fluid density, $\tau = tU_\infty/\ell_a$ is the non-dimensional time, $St_{\text{N}} = f_{\text{N}}\ell_a/U_\infty$ is the Strouhal number based on the natural frequency of the spring ($f_{\text{N}} = \frac{1}{2\pi}\sqrt{K/\mathcal{I}}$), $\xi = \frac{C}{2\sqrt{K\mathcal{I}}}$ is the non-dimensionalized damping parameter, t_a is the airfoil thickness, and C_M is the net pitching moment around the hinge based on the torque acting on the actuator.

In order to accurately compute the fluid-structure interaction problem, a coupled algorithm that solves the spring dynamics and the fluid-flow equations implicitly is needed. The computational algorithm used in this work for flow over immersed objects on simple Cartesian grids is based on a fictitious domain approach.[29] In this approach, the entire fluid-rigid body domain is assumed to be an incompressible, but variable density, fluid. The flow inside the fluid region is constrained to be divergence-free for an incompressible fluid, whereas the flow inside the particle (or rigid body) domain is constrained to undergo rigid body motion (i.e. involving translation and rotational motions only).

The momentum equations together with the incompressibility constraint are:

$$\frac{\partial u_j}{\partial x_j} = 0; \qquad \frac{\partial u_i}{\partial t} + \frac{\partial u_j u_i}{\partial x_j} = -\frac{1}{\rho}\frac{\partial p}{\partial x_i} + \frac{1}{\rho}\frac{\partial \tau_{ij}}{\partial x_j} + g_i + \frac{1}{\rho} F_{R,i} \tag{3}$$

where τ_{ij} is the viscous stress tensor, and $F_{R,i}$ is the rigidity constraint force *that is present only inside the particle region* to enforce the rigid body motion. These equations are solved using a *three-stage fractional step algorithm*. First, the momentum equations are solved everywhere without the rigidity constraint force, using symmetric, energy conserving discretization.[30] The incompressibility constraint is then imposed by solving a pressure Poisson equation (obtained by taking the divergence of the momentum equation). The resultant velocity field, at this stage satisfies the incompressibility constraint every where but may not lead to rigid-body motion within the solid region. The flowfield inside the solid region can be decomposed into a rigid body component ($\mathbf{u}^{RBM}$) and a deformational component ($\mathbf{u}'$); $\mathbf{u} = \mathbf{u}^{RBM} + \mathbf{u}'$, where $\mathbf{u}^{RBM} = \mathbf{U}_p^T + \mathbf{\Omega}_p \times \mathbf{r}$, RBM stands for rigid body motion consisting of translational ($\mathbf{U}_p^T$) and rotational components, $\mathbf{\Omega}_p$ is the angular rotation rate, and $\mathbf{r}$ is the position vector of an LP with respect to the immersed object centroid.

In the second stage, the RBM of the trailing edge can be obtained by solving the trailing edge dynamics equation (2) by decomposing it into two coupled first-order ODEs and using an explicit third-order Runge-Kutta scheme. The pitching moments are obtained from the velocity field computed in the above stage. Knowing the angular velocity of the trailing edge, the rigid body motion, $\mathbf{u}^{RBM} = \mathbf{U}_p^T + \mathbf{\Omega}_p \times \mathbf{r}$, can be

easily obtained by considering rotation around the hinge point. Finally, the rigidity constraint force (non-zero only inside the immersed object) is then computed and imposed in a third stage to make the velocity field inside the immersed object a rigid body motion:

$$\mathbf{F}_R = -\rho \mathbf{u}'/\Delta t. \tag{4}$$

In order obtain a strong coupling between the spring dynamics and the fluid-flow solver, the two sets of equations are solved iteratively in each time-step. In the numerical implementation, small material points/volumes of cubic shape that completely occupy the immersed object are created. Each material volume is assigned the properties of the immersed object (e.g. density etc.). The shape of the object can be reconstructed from these material volumes by computing an indicator or color function (with value of unity inside the object and zero outside) on a fixed background mesh used for flow solution.

The algorithm uses colocated grid formulation for velocity and pressure field, with symmetric, central differencing for momentum fluxes and eliminates the need for any upwind biased stencil for stability. All variables are stored at the control volume (cv) center with the exception of the face-normal velocity u_{N}, located at the face centers. The face-normal velocity is used to enforce continuity equation. Capital letters are used to denote material volume fields. Time-staggering is used so that the variables are located most conveniently for the time-advancement scheme. Accordingly, the material volume positions (X_i) are located at time level $t^{n-1/2}$ and $t^{n+1/2}$ whereas the velocity fields (u_i, u_{N}, and U_i) and the rigid body constraint force $f_{i,R}$, are located at time level t^n and t^{n+1}. This makes the discretization symmetric in time, a feature important to obtain good conservation properties. The iterative procedure within a single time-step is described below.

do while .NOT. done

1. Advance material point (MP) locations ($X_{i,P}^{n-1/2} \overset{U_{i,P}^n}{\frown\!\!\rightarrow} X_{i,P}^{n+1/2}$).
2. **for k = 1, N_inner_iters do**
   (a) **Solve momentum equations** (SOR) ($u_i^n \rightarrow \widehat{u}_i^k$)(Crank-Nicholson for inertial and viscous terms, latest pressure gradient)
   (b) **Setup and solve the pressure Poisson equation** (p_i^k) to impose the incompressibility constraint $\nabla \cdot u_i^{n+1}$ (algebraic multigrid, HYPRE). Compute face-based and cv-center pressure gradients (area-weighted pressure gradient reconstruction).
   (c) **Correct velocity**: face-based ($\widehat{u}_f^n \rightarrow u_f^k$) and cv-center velocity ($\widehat{u}_i \rightarrow u_i^k$).
   (d) **Interpolate** cv**-center velocity to MP-centers** (cv $\rightarrow$ MP) and **setup rigidity constraint force** base on latest velocity ($U_{i,P}^{RBM,k-1}$)
   (e) **Compute net torque** on the actuator around the hinge location and **solve the spring equations** (RK3): $\theta^n(\dot{\theta}^n) \rightarrow \theta^k(\dot{\theta}^k)$.
   (f) Compute new rigid body motion ($U_{i,P}^{RBM,k}$) and update the rigidity constraint force ($F_{i,P}^k$) based on new velocity.
   (g) **Impose rigidity constraint** within the rigid body using interpolation (MP $\rightarrow$ cv). Update cv-center velocity u_i^k.

   end for; set $u_i^{n+1} = u_i^k$; $U_{i,P}^{n+1} = U_{i,P}^n$.

Check if done; **end while**

The above approach has been implemented in a fully parallel, three-dimensional and conservative finite-volume scheme[31] for accurate prediction of turbulent flows. In order to verify the solver and also assess its predictive capability as applied to flow over airfoils over a range of Reynolds numbers [$\mathcal{O}(10^2 - 10^5)$], relevant to the operating conditions of micro-air vehicles, a systematic grid refinement study was performed on a standard test case of flow over SD7003 airfoil. The results are also compared with AFRL's very high-fidelity solver FDL3DI developed by Visbal.[12] For a fluid-structure interaction problem, the solver is also tested for a spring-mounted cylinder problem as described below.

III. Results

This section is arranged as follows. First, the computational studies involving verification tests as well as grid refinement studies on a SD7003 plunging airfoil and comparisons to the work by Visbal[12] are presented. Next, the canonical test case of flow over a spring-mounted cylinder is used to verify the capability of the solver to accurately capture the fluid-structure interactions. The verified solver is then applied to investigate the effect of a passively actuated trailing edge on the thrust and lift characteristics.

A. Verification Tests

The fictitious-domain approach was used to simulate flow over a plunging SD7003 airfoil, corresponding to the high-fidelity simulations by Visbal.[12] The case with chord Reynolds numbers of 10^3 and 10^4 were investigated. This test case is crucial to establish predictive capability of the present solver compared to AFRL's high-fidelity FDL3DI solver. In addition, it also allows to establish minimum grid resolution requirements to obtain grid converged results for flat airfoils studied next. The SD7003 airfoil has a maximum thickness of 8.5% and a maximum camber of 1.45% at 35% chord length. The original sharp trailing edge was rounded with a circular arc of radius ($r/c \approx 0.0004$, c is the chord length) corresponding to the simulations by Visbal.[12] The flow conditions correspond to angle of attack (α) of 4°, non-dimensional plunge amplitude $h_0 = 0.05$, reduced frequency of plunging motion, $k = \pi f c/U_\infty = 3.93$, where U_∞ is the free-stream velocity. A ramp function was used to allow smooth transition to the periodic plunging motion:

$$h(t) = h_0 \sin[2kF(t)t]; \quad F(t) = 1 - e^{-at}; \quad a = 4.6/t_0; \quad t_0 = 0.5. \tag{5}$$

Table 1. Grid and time-step resolutions for the SD7003 case used in present study (first three rows) and computations by Visbal[12] (bottom two rows).

Grid	$\Delta x/c$ (or $\Delta s/c$)	$\Delta y/c$ (or $\Delta n/c$)	$\Delta t U_\infty/c$
Baseline	0.00275	0.00275	0.0002
Coarse	0.005	0.005	0.0004
Non-uniform	0.005	0.0008	0.0002
Baseline[12]	0.005	0.00005	0.00005
Coarse[12]	0.01	0.001	0.0001

The grid resolution and time-step used for the present study are given in Table 1. A simple Cartesian grid refined in a small patch around the airfoil was used. Two grid points were used in the spanwise direction, with periodic conditions, for this two-dimensional study. Visbal[12] used a body-fitted, moving grid, and a sixth-order accurate algorithm with wall-normal resolution of 0.00005 and 0.0001 (non-dimensionalized by chord length) for baseline and coarse grids, respectively. The corresponding resolutions along the airfoil surface were 0.005 and 0.01, respectively. For the present simulations, a baseline grid resolution of 0.00275×0.00275 was used in axial and vertical directions. The grids were cubical whereas those used by Visbal were highly stretched in the wall-normal direction with very high aspect ratio. In the present study, a uniform coarse grid (twice as coarse compared to the baseline grid) was also used. In addition, non-cubic grids with much finer resolution in vertical direction compared to the axial direction were also used as shown in Table 1. Use of finer resolutions are feasible in the present solver; however, the simulations on thin, flat airfoil as planned in this study used similar resolutions as for the SD7003 case, in order to facilitate several parametric studies in reasonable time. The time-step used for the present incompressible flow simulations is also 4-times larger than those used by Visbal[12] in his compressible flow solver. The incompressible, pressure-based solver used in the present work allows for large time-steps (CFL $\sim$ 0.2) with good accuracy without any numerical instabilities.

Figure 3 shows contour plots of out-of-plane vorticity at four different phase angles (plotted at midspan) for $Re = 10,000$ compared with corresponding plots by Visbal[12] showing very good qualitative comparison of the vortex structures on the baseline grid. The phases shown correspond to the positions of maximum upward displacement (Phase 0), maximum downward velocity (Phase 1/4), maximum downward displacement (Phase 1/2), and maximum upward velocity (Phase 3/4). Due to large effective angle of attack induced by the

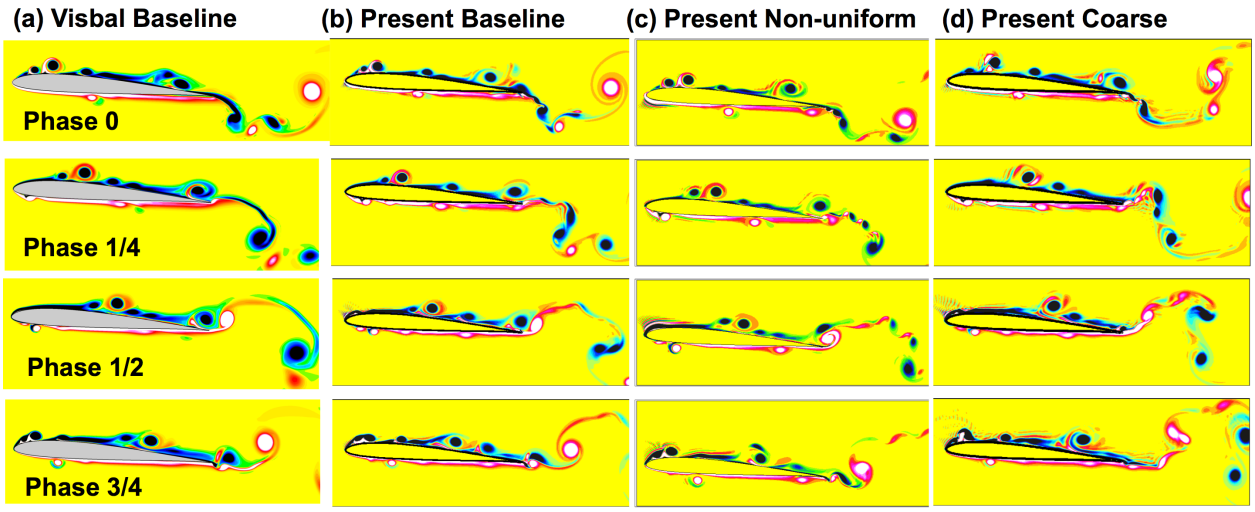

Figure 3. Instantaneous, out-of-plane vorticity contours ($\omega_z c/U_\infty$, range ± 40) for $Re = 10,000$: (a) results by Visbal[12] (on baseline grid), (b) present results on baseline grid, (c) present results on non-uniform grid, and (d) present results on coarse grid.

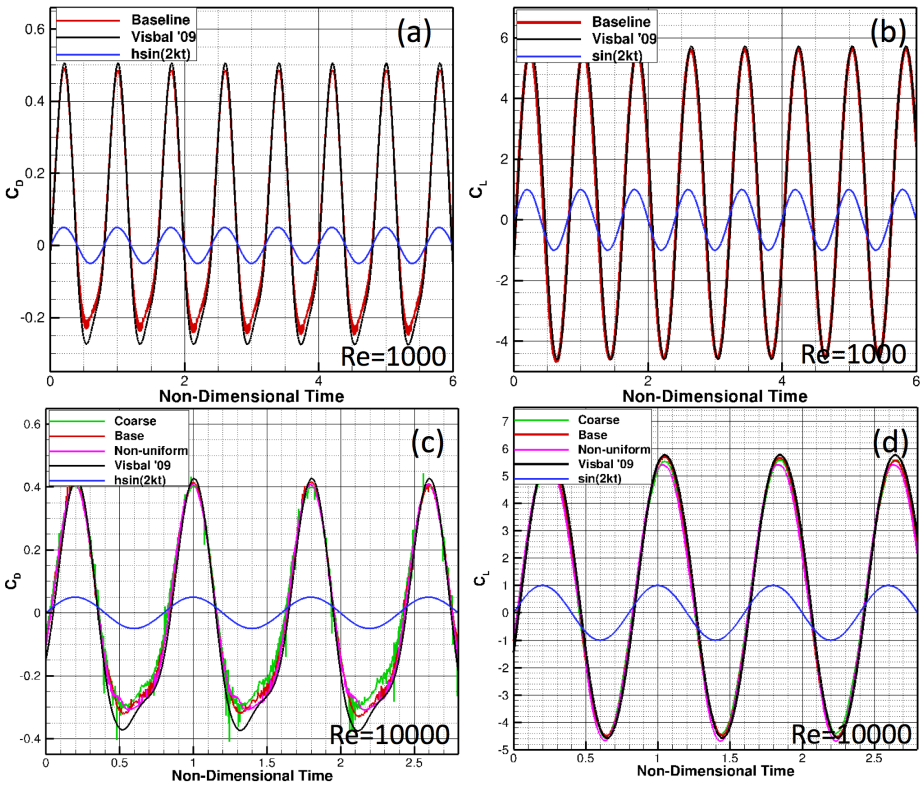

Figure 4. Two-dimensional loads on SD7003 airfoil at two different Reynolds numbers compared with the high-fidelity solver, FDL3DI:[12] (a,b) Drag and lift coefficients at $Re = 1000$, (c,d) drag and lift coefficients at $Re = 10000$. Predictions for baseline, coarse and non-uniform grids are shown.

plunging motion during the downward stroke, leading edge separation occurs on the upper surface creating coherent dynamic-stall-like vortices. Two distinct leading-edge vortices are formed above the upper surface. Owing to high-frequency of plunging, these leading edge vortices travel close to the upper surface and prevent stall conditions. Due to the vortex-surface interaction, ejection of vorticity of opposite sign from the upper surface is also observed similar to the work by Visbal. Formation of a single leading-edge vortex on the airfoil lower surface is also observed during the upstroke due to large negative angle of attack. All these features relate closely on the present baseline grid compared to those observed by Visbal. Some deviations of vortex structures in the wake region are observed for the non-uniform or coarse grids; however, around the airfoil surface, all grids seem to provide similar flow structures. This is further confirmed by comparing the temporal evolution of lift and drag coefficients for $Re = 1000$ and $Re = 10,000$.

Quantitative comparison of the lift and drag coefficients were also obtained for $Re = 10^3, 10^4$ as shown in figure 4. It is seen that, for both Reynolds numbers the loads are well predicted. The drag coefficient is slightly under-predicted for $Re = 10000$, near the phase 3/4 of the periodic cycle. This may be attributed to the coarser wall-normal resolution in the present simulations compared to those by Visbal.[12] However, the asymmetric nature of the drag coefficient (especially for $Re = 10000$) is captured by present simulations. This asymmetry actually results in mean thrust for these high-frequency plunging cases. This case study also verifies the predictive capability of the present solver on grids comparable to those used in the thin airfoil study described below.

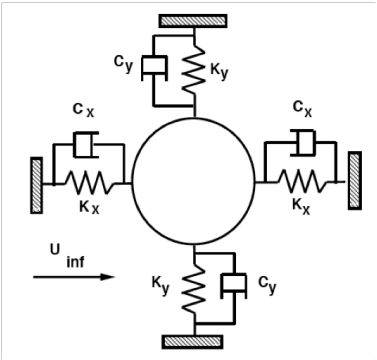

Figure 5. Spring mounted cylinder with two-degrees of freedom.

Flow over a spring-mounted cylinder with two-degrees of freedom has been studied extensively as a canonical test case for fluid-structure interaction problem.[32–35] The motion of the cylinder center (x_a, y_a) due to this fluid-structure coupling is governed by the following non-dimensionalized equations:

$$\frac{d^2x_a}{dt^2} + 4\pi\xi St_{\mathrm{N}}\frac{dx_a}{dt} + (2\pi St_{\mathrm{N}})^2 x_a = \frac{2}{\pi m^*}C_D \tag{6}$$

$$\frac{d^2y_a}{dt^2} + 4\pi\xi St_{\mathrm{N}}\frac{dy_a}{dt} + (2\pi St_{\mathrm{N}})^2 y_a = \frac{2}{\pi m^*}C_L, \tag{7}$$

where $f_{\mathrm{N}} = f_{\mathrm{N}x,y} = \frac{1}{2\pi}\sqrt{(K_{x,y}/m)}$, $St_{\mathrm{N}} = \frac{f_{\mathrm{N}}D}{U_\infty}$, $\xi = \xi_{x,y} = \frac{C_{x,y}}{2\sqrt{mK_{x,y}}}$, $m^* = m_c/m_f = m_c/(\pi/4\rho_f D^2)$, m_c is the cylinder mass, D is the cylinder diameter, and C_D, C_L are the drag and lift coefficients, respectively.

For flow over cylinder at $Re = 200$, the computational domain chosen was 30 times larger than the cylinder diameter in the x and y directions. Two grid cells were used in the spanwise direction with periodic boundary conditions. A uniform Cartesian grid was used around the cylinder center in a small patch to have well-resolved cylinder surface. The grid was stretched away from the cylinder. Three grid resolutions were used around the cylinder: $D/33$ (coarse), $D/66$ (medium) and $D/83$ (fine). Time step used is 1.8×10^{-3}, giving a CFL number of around 0.2 for the fine grid. First, flow over a rigid cylinder at $Re = 200$ was computed providing vortex shedding with a Strouhal number, $St = 0.1986$. The natural frequency of the spring was set based on this vortex shedding frequency by using $St_{\mathrm{N}} = St$.

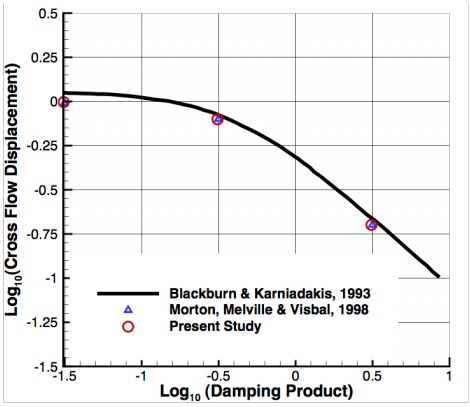

Figure 6. Cross-stream displacement for different damping coefficients compared to published data.

Multiple inner iterations per time-step were used to solve the fluid-structure interaction problem. It was found that, 3 and 5 inner iterations provided virtually identical solutions. With no inner iterations, the solution significantly over-predicted the cross-stream displacement of the cylinder. In all future simulations, three inner iterations were used. Figure 6 shows comparison of the cross-stream displacement of the cylinder center with other approaches based on spectral predictions by Blackburn & Karniadakis[33] and body-fitted, deforming grid algorithm of Morton *et al*[32] for different damping coefficients. Excellent prediction is obtained

using the present scheme. Other statistics such as variations in drag and lift coefficients were also predicted well compared to these studies.[35]

B. Passively Actuated Trailing Edge

A thin, flat, two-dimensional wing is selected in order to study the effect of passively actuated trailing edge on the flow dynamics. The wing is based on an existing physical model developed at Oregon State University for future experimental studies.[36,37] The chord length (c) is 20 cm, the thickness to chord ratio is 0.038, the actuator length to chord ratio is 0.3, and a span to chord ratio is 3.85. The airfoil has elliptical rounded edges with a height to length ratio of 1:5.

The numerical model of the airfoil was created by distributing material points along the surface of the airfoil. The airfoil surface was defined by breaking the airfoil up into simpler shapes. The entire airfoil is generated at an angle of attack of zero with an actuator angle of zero. The material points are then rotated to the appropriate angle of attack. The five component shapes are an ellipse for the trailing edge, a line segment for the body of the airfoil, a semicircle for the hinge joint, a line segment for the flap body, and an ellipse for the leading edge. The origin for the airfoil is located at the trailing edge with the front of the airfoil pointed to the left (negative x direction). Due to the symmetry of the airfoil, for each point placed on the top surface of the airfoil, another is placed on the bottom surface by mirroring the top point across the x-axis. The airfoil is given depth by copying the points from the first cross-section to make additional cross-sections in the spanwise direction. The ellipses for the leading and trailing edges are generated using the following equation for an ellipse, the thickness of the airfoil, and the ratio of length to height:

$$\frac{(x - x_o)^2}{\frac{1}{2} r t_c^2} + y^2/t_c^2 = 1, \tag{8}$$

where x_o is the x location of the center of the ellipse, r is the length-to-height ratio (5 in this case) of the ellipse, and t_c is the thickness of the airfoil. The x locations of the material points are spaced evenly between the tip of the ellipse and the center. The y location is solved for using the above equation. The x_c for the trailing edge and leading edge are $(-t_c r/2)$ and $(t_c r/2c)$, respectively, where c is the chord length. Next the flat airfoil and actuator sections are added. Each flat section is generated by equally spacing material points along the flat surface. The airfoil flat surface extends from the end of the trailing edge ellipse to the start of the actuator hinge, and similarly, from the end of the actuator hinge to the end of the leading edge ellipse. Next the hinge material points are added. The hinge height and width are equal to the thickness of the airfoil. The hinge is formed by fitting two semi-circles into the gap between the airfoil surface and the flap surface. The semicircles are created tangent to both the flap and airfoil surfaces to create a smooth transition. The upper and lower semicircles are concentric. While adding the semi-circle to the underside of the airfoil does not match the shape of an actual hinge, the benefit is that the front actuator can be moved smoothly without the need to add material points. The final step is to rotate all the material points around the trailing edge by the specified angle of attack. Grid resolutions used in the present calculations are given in Table 2. The baseline resolution is finer than that used for corresponding studies on the plunging SD7003 as discussed earlier.

Table 2. Cartesian grid resolution and time-steps for thin, flat airfoil studies.

Grid	$\Delta x/c$	$\Delta y/c$	$\Delta t U_\infty/c$
Baseline	0.0015	0.0015	0.0001

The thin, flat wing with spring-mounted trailing edge, gives rise to a wide range of physical and operational parameters. The main physical parameters are the trailing edge actuator size (ℓ_a/c), the torsion spring parameters including spring stiffness (K) and damping (C) that can be expressed in the non-dimensional form as $St_N = f_N \ell_a/U_\infty$ and $\xi = C/2\sqrt{K/\mathcal{I}_a}$, respectively. Here $f_N = 1/(2\pi)\sqrt{K/\mathcal{I}_a}$ is the natural frequency of the spring, $\mathcal{I}_a$ is the moment of inertial of the trailing edge actuator which can also be expressed as moment of inertia ratio $\mathcal{I}^* = \rho_a/\rho_f$. There are also several operational parameters such as the flow Reynolds number, $Re = U_\infty c/\nu$, angle of attack (α_0), the plunging amplitude ($h = a_{LE}/c$), the plunging frequency ($k = \pi f_p c/U_\infty$) and the plunging waveform. In the present proof-of-concept work, only a small parameter space is explored, wherein for a certain fixed operational parameter, the spring flexibility (i.e f_N) is varied

and its effect on the performance of the foil is investigated. The parameters chosen for this study are given in Table 3. The parameter space is based on plunging frequency (f_p) of 10 Hz. The spring constants are varied such that the natural frequencies are 5, 8, 10, 12.5, and 20 Hz. The results are compared with a non-actuated trailing edge, that is a very stiff spring ($f_\mathrm{N} \to \infty$).

Table 3. Parameter space investigated in present study.

ℓ_a/c	St_N	ξ	I^*	Re	α_0	h	k
0.3	0, 0.27, 0.43, 0.54, 0.68, 1.09	0.01	8.4	14700	5°	0.05	5.7

The plunging oscillation was a simple sinusoidal oscillation given as,

$$h(t) = \frac{a_\mathrm{LE}}{c}\sin(2kt), \tag{9}$$

where a_LE is the amplitude of the leading edge. With the above parameters, a plunging airfoil without any tail actuation, the airfoil results in a small mean drag; $\bar{C}_D = 0.0164$ with a mean lift coefficient of $\bar{C}_L = 0.645$. More than 10 complete cycles of plunging were computed before the passive actuation was initiated and the spring natural frequencies were varied to study effect of spring flexibility on the drag and lift coefficients, as well as performance of the foil.

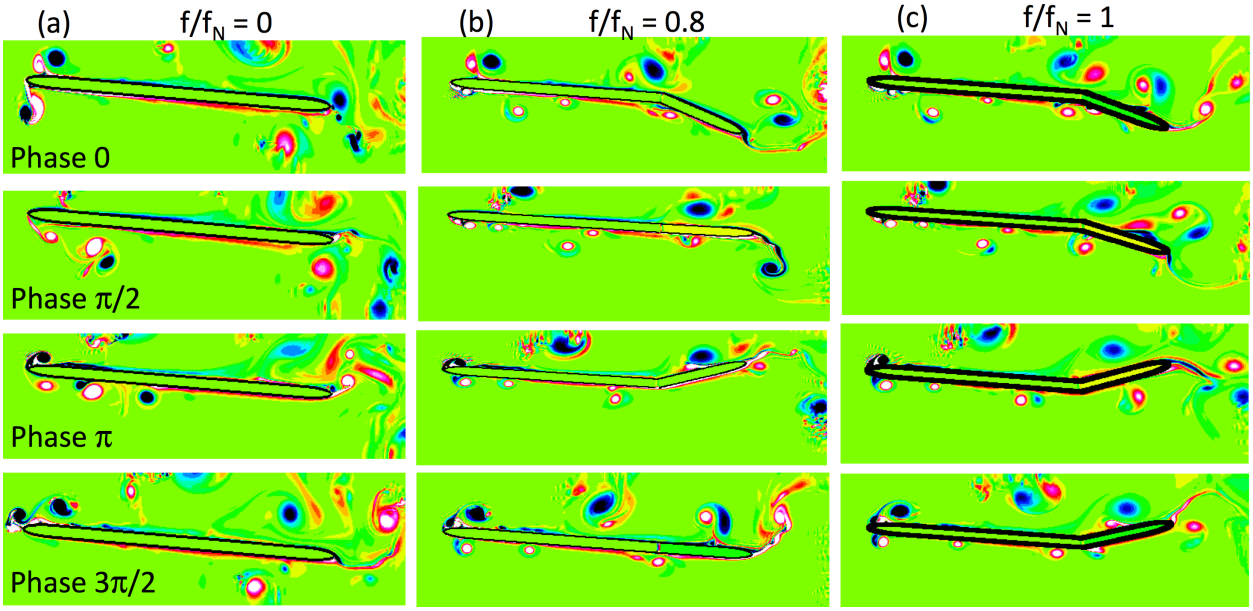

Figure 7. Temporal out-of-plane vorticity contours for one period of plunging motion: (a) $f_p/f_\mathrm{N} = 0$ (no actuation); (b) $f_p/f_\mathrm{N} = 0.8$, and (c) $f_p/f_\mathrm{N} = 1$. Phase 0 is the center position going up, phase $\pi/2$ is top-most position, phase π is center position going down, and phase $3\pi/2$ is bottom most position.

Figure 7 shows the out-of-plane vorticity contours for four different phases for a single plunging cycle for $f_p/f_\mathrm{N} = 0$ (no actuation), $0.8, 1$. The plots show positions of the trailing edge tip with passive actuation compared to the corresponding positions with simple plunging motion. For $f/f_\mathrm{N} = 0.8$, starting with phase 0 (center position of the airfoil), the trailing edge is at its lowest downward position. From phase 0 to $\pi/2$, the leading edge is rising upward and reaches the top most position at phase $\pi/2$. The trailing edge, starting from its lowest position also rises upwards (rotates counter-clockwise) and is perfectly aligned with the leading edge at the top-most position. Between phase $\pi/2$ to π, the leading edge starts its downward motion, whereas the trailing edge is still rising (rotating counter-clockwise). Starting from phase π (the center position), the leading edge continues to move downward and reaches its lowest point at $3\pi/2$. Between this section, the trailing edge also starts its downward motion (rotates clock-wise) and aligns perfectly with the leading edge at $3\pi/2$. When the plunging frequency and the spring natural frequency match, the displacement of the trailing edge is the largest as seen from the extent of the trailing edge tip for $f_p/f_\mathrm{N} = 1$. When compared with the pure plunging case ($f_p/f_\mathrm{N} = 0$), the vorticity contours near the trailing edge for actuated cases are considerably altered as the motion of an actuated trailing edge dynamically pushes fluid away from the

surface. It is also interesting to note that, the vorticity contours even near the leading edge are different between cases with and without trailing edge actuation.

Figure 8 compares the relative amplitude of an actuated trailing edge (s_{TE}) compared to that of a non-actuated (very stiff spring) trailing edge ($s_{\mathrm{TE,rigid}}$) non-dimensionalized by the amplitude of plunging motion (a_{LE}) for various spring natural frequencies. Also shown is waveform of the pure-plunging motion for comparison. The positive peak of the sine wave represents top most position of the trailing edge whereas the negative peak is the bottom most position. It is observed that the resonant frequency case ($f_p/f_{\mathrm{N}} = 1$) results in the largest amplitude as expected. For $f_p/f_{\mathrm{N}} = 0.8$, the trailing edge tip is 90° out of phase of the leading edge. Phase difference for the resonant case of $f_p/f_{\mathrm{N}} = 1$ is slightly lower.

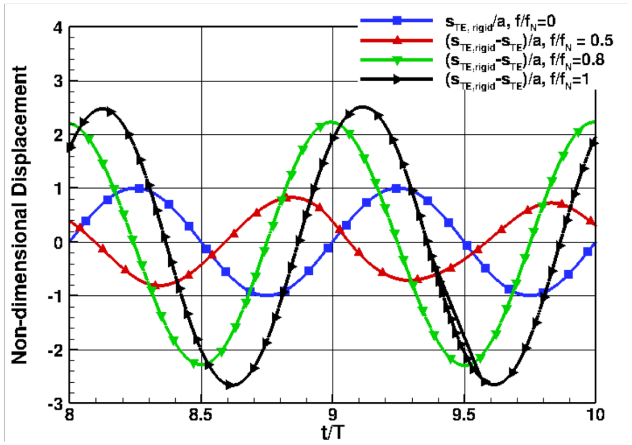

Figure 8. Non-dimensionlized relative motion of the trailing edge tips for various flexibility level of the torsion spring compared with the pure plunging case. Also shown is the sinusoidal signal of the trailing edge motion (blue line).

To investigate the effect of the trailing edge actuation on the drag force, the temporal variation of the drag coefficient for the trailing edge actuator as well as the trailing edge displacement (θ) are plotted in figure 9 for $f_p/f_{\mathrm{N}} = 0.8$ and 1 together with pure plunging case. It is observed that for the pure plunging case, the trailing edge drag coefficient remains positive for much of the duration of the cycle and leads to a net mean drag. However, for spring actuation with $f_p/f_{\mathrm{N}} = 0.8$, the drag coefficient on the trailing edge reverses trend, and remains negative for a major part of the cycle, resulting in a net thrust. The corresponding plots for $f_p/f_{\mathrm{N}} = 1$ show also reduced drag coefficient compared to pure plunging case, but a net mean thrust is not obtained for this case.

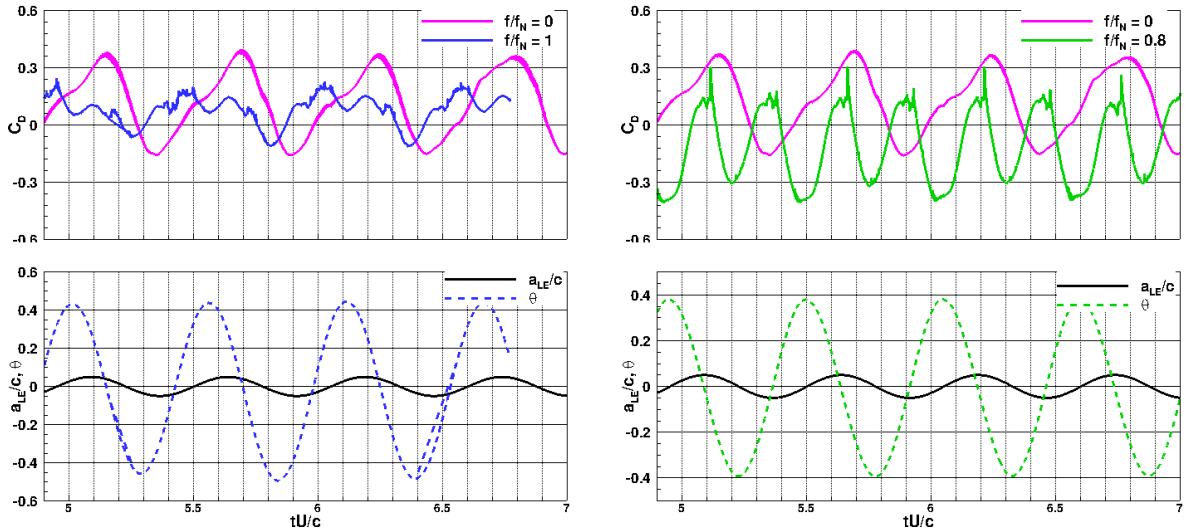

(a) (b)

Figure 9. Temporal variation of the drag coefficient of the trailing edge and actuator angle (θ) over few cycles of plunging motion: (a) $C_{D,\mathrm{actuator}}$ and θ for $f_p/f_{\mathrm{N}} = 0.8$; (b) $C_{D,\mathrm{actuator}}$ and θ for $f_p/f_{\mathrm{N}} = 1$. Also shown is the drag coefficient for no actuation case ($f_p/f_{\mathrm{N}} = 0$) and the sinusoidal motion of the leading edge.

Table 4 lists the effect of increased flexibility of the torsion spring and passive actuation of the tail on the drag and lift coefficients, as well as the propulsion efficiency. The propulsion efficiency is defined as:

$$\eta = -\frac{\overline{F}_D U_\infty}{\overline{F_L v}} = -\frac{\overline{C_D}}{\overline{C}_{\mathrm{prop}}}; \quad \overline{C}_{\mathrm{prop}} = \frac{\overline{F_L v}}{\frac{1}{2}\rho U_\infty^3 c}, \tag{10}$$

where the negative sign is because the force considered is drag (instead of thrust)and $\overline{C}_{\text{prop}}$ is the average power input for the plunging motion. Here, v is the vertical velocity due to plunging motion. The first column f_p/f_{N} provides the ratio of plunging frequency to the spring natural frequency, starting from 0 (i.e. rigid spring, no actuation) to increasing flexibility. The second column lists the ratio of the amplitude of the leading edge (mainly following the plunging motion) to the trailing edge (consisting of plunging motion together with motion due to actuation of the trailing edge). For $f_p/f_{\text{N}} = 1$, a resonance effect is expected and one obtains the largest variation in the amplitude ratios. Next four columns list the mean drag and lift coefficients on the trailing edge actuator and on the entire airfoil, respectively. It is observed that the rigid tail gives small positive mean drag in the absence of any actuation. With passive actuation and increasing flexibility ($f_p < f_{\text{N}}$), mean thrust is obtained, whereas the mean lift coefficient also increases slightly. Further increase in flexibility ($f_{\text{N}} \leq f_p$) shows increase in mean drag on the airfoil. It is also observed that for $f_p/f_{\text{N}} = 0.5$ and 0.8, the trailing edge actuator itself produces thrust and resultant thrust for the entire wing is large. With increase in flexibility of the spring, the trailing edge actuator actually results in more drag than the overall wing, indicating that with increase in flexibility, the tail moves in a position relative to the leading edge that is not beneficial for the system. The last column lists the propulsion efficiency. For $f_p/f_{\text{N}} = 0.5$ and 0.8, net positive efficiency (thrust) is obtained for otherwise negative efficiency without any actuation. This suggests that there exists a range of flexibility that improves performance of the flapping wing, whereas too much flexibility can affect the efficiency adversely.

Table 4. Effect of passively actuated tail flap on performance of a plunging foil: $k = \frac{\pi f c}{U_\infty} = 5.71$, (f = 10 Hz) $\alpha_0 = 5°$, $Re_c = 14700$, $I^* = 8.4$, $\xi = 0.01$.

f_p/f_{N}	$a_{\text{TE}}/a_{\text{LE}}$	Actuator $\bar{C}_D$	Actuator $\bar{C}_L$	$\bar{C}_D$	$\bar{C}_L$	$\bar{C}_{\text{prop}}$	η
0 (rigid)	1.0	+0.1103	0.059	+0.0164	0.645	0.556	-0.032
0.5	0.815	-0.014	0.0693	-0.1	0.662	0.83	+0.133
0.8	2.24	-0.11	0.1	-0.162	0.7245	0.729	+0.244
1	2.58	+0.0715	0.13	+0.071	0.65	0.237	-0.33
1.25	2.045	+0.165	-0.067	+0.12	0.044	0.118	-1.18
2	1.245	+0.167	-0.035	+0.122	0.333	0.178	-0.76

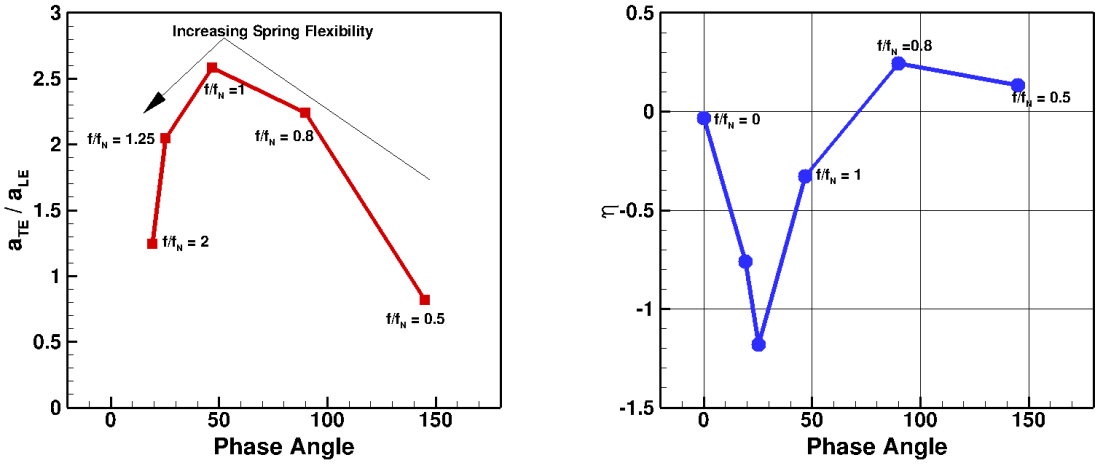

Figure 10. Effect of spring flexibility on (a) non-dimensional trailing edge amplitude variation and (b) propulsion efficiency and their correlation with phase difference between the leading and trailing edge motion due to passive actuation.

Figure 10a shows the effect of spring flexibility on the amplitude of trailing edge motion in comparison with the leading edge and corresponding phase difference between the leading and trailing edges. Similar plot of propulsion efficiency versus phase difference is given in figure 10b. It is observed that the amplitude

of trailing edge fluctuation is maximum for the resonant case of matching plunging frequency and spring natural frequency, $f_p = f_N$. With increasing spring flexibility (i.e. smaller f_N), the amplitude of trailing edge oscillation decreases and approaches the pure plunging amplitude. Similarly, the phase difference between the leading and trailing edge motion also decreases with increasing flexibility. However, it observed that with increasing flexibility ($f_p/f_N \geq 1$), the propulsion efficiency is negative, that is a net mean drag is obtained. The propulsion efficiency is maximum when the phase difference between the leading and trailing edges is 90°. This occurs for $f_p/f_N = 0.8$ in the present case. It is also observed that peak amplitude of trailing edge fluctuation does not correspond to the peak performance. Peak performance is more dependent upon the phase difference between the leading and trailing edge motions. To better understand these observations, the four phases of plunging motion with and without actuation are compared below.

- Phase 0: At this point, the leading edge is at its center position and is rising up. It is observed that the trailing edge actuator has the maximum positive θ for $f_p/f_N = 0.8$ (i.e. the trailing edge tip is below the corresponding tip for no-actuation case) and corresponding negative C_D on the trailing edge actuator. For no actuation (or rigid tail), the drag coefficient at this position is nearly zero. For $f_p/f_N = 1$, the actuator angle is positive but lower than its maximum value, whereas the drag coefficient is also positive.
- Phase $\pi/2$, (maximum positive a_{LE}/c): At this point, the trailing edge has reached its top-most position and getting ready to start moving downwards. It is observed that for $f_p/f_N = 0.8$, the flap angle is decreasing and reached $\theta = 0$, i.e. trailing edge moved upward and is coinciding with the trailing edge of a no actuation case. At this stage there is small positive drag on the trailing edge actuator. For $f_p/f_N = 1$, the trailing edge is still moving upwards but is below the corresponding rigid airfoil edge. This also results in positive drag.
- Phase π: At this point, the trailing edge has reached its center position again and getting ready to start moving further downward. It is observed that for $f_p/f_N = 0.8$, the flap angle has reached its highest negative value, i.e. trailing edge continued to move upward and is now further up compared to the trailing edge of a no actuation case. At this stage there is again negative drag (thrust). For $f_p/f_N = 1$, the trailing edge is also moving upwards and a negative drag (thrust) is obtained.
- Phase $3\pi/2$: At this point, the trailing edge has reached its lowest position and getting ready to start moving upward. It is observed that for $f_p/f_N = 0.8$, the flap angle is zero, i.e. trailing edge continued to move downward and is now coinciding with the trailing edge of a no actuation case. At this stage there is again small positive drag. For $f_p/f_N = 1$, the trailing edge is moving downwards and still above the trailing edge without no actuation. This also results in positive drag.

The four phases of the airfoil cycle indicate that, for $f_p/f_N = 0.8$, the trailing edge actuator adds an additional kicking motion that results in displacing the fluid away from the airfoil. Together with the plunging motion the cumulative of the trailing edge oscillation is to provide a resultant thrust on the airfoil. The case with $f_p/f_N = 1$ also has similar effect, but lags in its position of the trailing edge tip and results in a small net drag.

IV. Conclusion

Effect on airfoil performance due flow-induced passive actuation of a spring-mounted trailing edge at low Reynolds number was investigated using two-dimensional DNS studies. The trailing edge, attached with a torsion spring at 30% the chord length, is modeled as a spring-mounted compound pendulum with single-degree of freedom. It may undergo flow induced rotation resulting in dynamic variations in the effective airfoil shape. A second-order, fictitious domain method[29] was further extended to account for flow-structure interaction problems and verified to show good predictive capability, compared to AFRL's flow-structure interaction solver (FDL3DI).[12]

Of particular importance is application of the spring-mounted trailing edge actuator concept to a plunging wing. High-frequency, low amplitude plunging is used to approximate wing motion in a flapping wing design. It should be noted that, in this study there is no explicitly imposed pitching motion of the wing. However, an implicit pitching like motion is present owing to flow-induced rotation of the trailing edge. This model problem involves a single degree of freedom for the trailing edge motion but introduces several parameters. The main physical parameters are the length of the trailing edge actuator compared to the chord length

(ℓ_a/c), the actuator moment of inertia ($\mathcal{I}_a$), the spring stiffness (K) governing its natural frequency ($f_{\rm N}$), and spring damping coefficient (C). The main operational parameters are the flow Reynolds number (Re), the angle of attack (α_0), the pitching amplitude ($h = a_{\rm LE}/c$), and the pitching waveform (reduced frequency k and shape). Although a systematic parametric study over a wide range of parameter space is necessary to investigate the effect of passive actuation on wing performance, only a small parameter space is explored in this work.

Effect of trailing edge actuation on a sinusoidally plunging ($k = 5.71$, $h = 0.05$) thin, flat airfoil was investigated at 5° angle of attack. For the parameters chosen, without any actuation (extremely stiff spring), the foil resulted in a small net positive drag in the mean. By introducing some spring flexibility, the drag coefficient decreased and lift coefficient increased resulting in better performance of the wing. For certain spring parameters resulting in spring natural frequencies slightly larger than the plunging frequency ($f_p/f_{\rm N} = 0.5 - 0.8$), dramatic increase in performance was observed. The wing motion resulted in thrust and higher lift coefficients with a propulsive efficiency as high as 24.4%. It was found that most increase in propulsive efficiency was obtained when the trailing edge tip was 90° out-of-phase with the leading edge, an observation consistent with experimental data on plunging teardrop airfoils with flexible tail filament by Heathcote and Gursul.[5,11,38] It was also observed that, there exists a range of spring flexibility that results in enhanced performance (increased thrust and/or propulsive efficiency). However, too much flexibility of the spring can adversely affect performance, again a consistent result similar to observations on purely flexible trailing edge filament. The advective time scales (c/U_∞), the plunging time scale ($1/f_p$) and the spring flexibility time scale ($1/f_{\rm N}$) play a major role in governing the dynamics of the passively actuated trailing edge. Future work will involve variation of the flow Re as well as plunging waveforms and amplitudes to investigate the correlations between these time scales and airfoil performance. In addition, a physical setup of a two-dimensional passively actuated trailing edge wing is being built to measure lift, drag, and pitching moments together with detailed time-resolved, three-component PIV studies in a wind-tunnel at Oregon State University.

This proof-of-concept work suggests that use of a single-degree of freedom spring-mounted trailing edge and resultant passive control can be used as a simplified canonical mechanism to study effect of trailing edge flexibility on flapping wing design. The results are of direct relevance to other forms of flow control which are more amenable to small scale MAV implementation; for example, surface deformations via piezo-electric actuators or aero-elastically tailored structures. Use of trailing edge actuators (either actively or passively controlled) provide an effective way to increase foil performance and provide means to control the lift and drag characteristics under transient maneuvers or flow disturbances.

V. Acknowledgements

Part of this work was conducted at Wright Patterson Airforce Base under the AFOSR's ASEE-Summer Faculty Fellowship Program. SVA gratefully acknowledges summer research support during 2010 and 2011 under this program. MV acknowledges AFOSR support under task monitored by Dr. Doug Smith. We also acknowledge useful discussions with Dr. Justin Jaworski of University of Cambride (formerly at Wright Patt). We also thank Mr. Kevin J. Drost, for developing the algorithm for the the thin-flat plate airfoil motion with elliptically rounded edges.

References

[1]Shyy, W., Berg, M., and Ljungqvist, D., "Flapping and flexible wings for biological and micro air vehicles," *Progress in Aerospace Sciences*, Vol. 35, No. 5, 1999, pp. 455–505.

[2]Ho, S., Nassef, H., Pornsinsirirak, N., Tai, Y., and Ho, C., "Unsteady aerodynamics and flow control for flapping wing flyers," *Progress in Aerospace Sciences*, Vol. 39, No. 8, 2003, pp. 635–681.

[3]Jones, K. and Platzer, M., "Design and development considerations for biologically inspired flapping-wing micro air vehicles," *Experiments in fluids*, Vol. 46, No. 5, 2009, pp. 799–810.

[4]Triantafyllou, M., Triantafyllou, G., and Yue, D., "Hydrodynamics of fishlike swimming," *Annual review of fluid mechanics*, Vol. 32, No. 1, 2000, pp. 33–53.

[5]Heathcote, S., Wang, Z., and Gursul, I., "Effect of spanwise flexibility on flapping wing propulsion," *Journal of Fluids and Structures*, Vol. 24, No. 2, 2008, pp. 183–199.

[6]Mackenzie, D., "A Flapping of Wings," *Science*, Vol. 335, No. 6075, 2012, pp. 1430–1433.

[7]Molki, M. and Breuer, K., "Oscillatory motions of a prestrained compliant membrane caused by fluid-membrane interaction," *Journal of Fluids and Structures*, Vol. 26, No. 3, 2010, pp. 339–358.

[8]Hubel, T., Riskin, D., Swartz, S., and Breuer, K., "Wake structure and wing kinematics: the flight of the lesser dog-faced fruit bat, Cynopterus brachyotis," *Journal of Experimental Biology*, Vol. 213, No. 20, 2010, pp. 3427–3440.

[9]Riskin, D., Iriarte-Díaz, J., Middleton, K., Breuer, K., and Swartz, S., "The effect of body size on the wing movements of pteropodid bats, with insights into thrust and lift production," *Journal of Experimental Biology*, Vol. 213, No. 23, 2010, pp. 4110–4122.

[10]Platzer, M. and Jones, K., "Flapping wing aerodynamics-progress and challenges," *44th AIAA Aerospace Sciences Meeting and Exhibit; Reno, NV; USA*, 2006, pp. 1–19.

[11]Heathcote, S., Martin, D., and Gursul, I., "Flexible flapping airfoil propulsion at zero freestream velocity," *AIAA journal*, Vol. 42, No. 11, 2004.

[12]Visbal, M., "High-fidelity simulation of transitional flows past a plunging airfoil," *AIAA Journal*, Vol. 391, 2009, pp. 2009.

[13]Visbal, M., Gordnier, R., and Galbraith, M., "High-fidelity simulations of moving and flexible airfoils at low Reynolds numbers," *Experiments in Fluids*, Vol. 46, No. 5, 2009, pp. 903–922.

[14]Katz, J. and Weihs, D., "Hydrodynamic propulsion by large amplitude oscillation of an airfoil with chordwise flexibility," *J. Fluid Mech*, Vol. 88, No. 3, 1978, pp. 485–497.

[15]Murray, M. and Howle, L., "Spring stiffness influence on an oscillating propulsor," *Journal of fluids and structures*, Vol. 17, No. 7, 2003, pp. 915–926.

[16]Miao, J. and Ho, M., "Effect of flexure on aerodynamic propulsive efficiency of flapping flexible airfoil," *Journal of Fluids and Structures*, Vol. 22, No. 3, 2006, pp. 401–419.

[17]Gordnier, R., Visbal, M., and Garmann, D., "High-Fidelity Computations for Flexible Micro Air Vehicle Applications," *High Performance Computing Modernization Program Users Group Conference (HPCMP-UGC), 2010 DoD*, IEEE, 2010, pp. 26–34.

[18]Meyer, R., Hage, W., Bechert, D., Schatz, M., Knacke, T., and Thiele, F., "Separation control by self-activated movable flaps," *AIAA journal*, Vol. 45, No. 1, 2007, pp. 191–199.

[19]Schlüter, J., "Lift Enhancement at Low Reynolds Numbers using Pop-Up Feathers," 2009.

[20]Jones, K., Duggan, S., and Platzer, M., "Flapping-wing propulsion for a micro air vehicle," *AIAA Paper*, Vol. 126, 2001.

[21]Toomey, J. and Eldredge, J., "Numerical and experimental investigation of the role of flexibility in flapping wing flight," *AIAA Paper*, Vol. 3211, 2006, pp. 2006.

[22]Toomey, J. and Eldredge, J., "Numerical and experimental study of the fluid dynamics of a flapping wing with low order flexibility," *Physics of Fluids*, Vol. 20, No. 7, 2008, pp. 073603–073603.

[23]Heathcote, S. and Gursul, I., "Flexible flapping airfoil propulsion at low Reynolds numbers," *AIAA journal*, Vol. 45, No. 5, 2007, pp. 1066–1079.

[24]Eldredge, J., Toomey, J., and Medina, A., "On the roles of chord-wise flexibility in a flapping wing with hovering kinematics," *Journal of Fluid Mechanics*, Vol. 659, 2010, pp. 94–115.

[25]Mueller, T. and DeLaurier, J., "An overview of micro air vehicle aerodynamics.' Fixed and flapping wing aerodynamics for micro air vehicle applications," *Progress in Astronautics and Aeronautics*, Vol. 195, 2001, pp. 1–10.

[26]Hoarau, Y., Braza, M., Ventikos, Y., Faghani, D., and Tzabiras, G., "Organized modes and the three dimensional transition to turbulence in the incompressible flow around a NACA0012 wing," *J. Fluid Mech.*, Vol. 496, 2003, pp. 63–72.

[27]Nishimura, H. and Taniike, Y., "Aerodynamic characteristics of fluctuating forces on a circular cylinder," *J. Wind Eng., Ind. Aerodynamics*, Vol. 89, 2001, pp. 713–723.

[28]Sicot, C., Auburn, S., Loyer, S., and Devinant, P., "Unsteady characteristics of the static stall of an airfoil sujected to freestream turbulence level up to 16%," *Exp. in Fluids*, Vol. 41, 2006, pp. 641–648.

[29]Apte, S., Martin, M., and Patankar, N., "A numerical method for fully resolved simulation (FRS) of rigid particle-flow interactions in complex flows," *Journal of Computational Physics*, 2008, pp. doi:10.1016/j.jcp.2008.11.034.

[30]Mahesh, K., Constantinescu, G., and Moin, P., "A new time-accurate finite-volume fractional-step algorithm for prediction of turbulent flows on unstructured hybrid meshes," *J. Comp. Phy.*, Vol. 197, 2004, pp. 215–240.

[31]Moin, P. and Apte, S., "Large eddy simulation of multiphase reacting flows in complex combustors," *AIAA J. (special issue on 'Combustion Modeling and LES: Development and Validation Needs for Gas Turbine Combustors)*, Vol. 44, 2006, pp. 698–710.

[32]Morton, S., Melville, R., and Visbal, M., "Accuracy and coupling issues of aeroelastic Navier-Stokes solutions on deforming meshes," *Journal of aircraft*, Vol. 35, No. 5, 1998, pp. 798–805.

[33]Blackburn, H. and Karniadakis, G., "Two-and three-dimensional simulations of vortex-induced vibration of a circular cylinder," *Proceedings of the Third International offshore and polar engineering conference*, Citeseer, 1993.

[34]Yang, J., Preidikman, S., and Balaras, E., "A strongly coupled, embedded-boundary method for fluid-structure interactions of elastically mounted rigid bodies," *Journal of Fluids and Structures*, Vol. 24, No. 2, 2008, pp. 167–182.

[35]Kim, D. and Choi, H., "Immersed boundary method for flow around an arbitrarily moving body," *Journal of Computational Physics*, Vol. 212, No. 2, 2006, pp. 662–680.

[36]Drost, K., Johnson, H., Apte, S., and Liburdy, J., "Low Reynolds number flow dynamics of a thin airfoil with an actuated leading edge," *AIAA-2011-3944, 41st AIAA Fluid Dynamics Conference*, American Institute of Aeronautics and Astronautics, Honolulu, HI, USA, 2011.

[37]Drost, K., "Direct Numerical Simulation of a Flat Wing with a Movable Front Flap at High Angles of Attack and Low Reynolds Numbers," *University Honors College B.S. Thesis, Oregon State University*, 2010.

[38]Heathcote, S. and Gursul, I., "Jet switching phenomenon for a periodically plunging airfoil," *Physics of Fluids*, Vol. 19, 2007, pp. 027104.